



High-performance martensitic stainless steel nanocomposite powder for direct energy deposition prepared by ball milling

Zhen Wang, Shu-Rong Xu, Qing-Xuan Sui, Jiang Wang, Bo Liu, Hao Wen, Tian-Yi Xiao, Quan Yuan, Feng-Jun Zhao, Jun Liu* 

Received: 11 August 2022 / Revised: 14 September 2022 / Accepted: 22 September 2022 / Published online: 29 March 2023
© Youke Publishing Co., Ltd. 2023

Abstract Direct energy deposition (DED) has great potential for the production of stainless steel matrix nanocomposite parts. However, the propensity of nanoparticle agglomeration leads to the difficulty in realizing homogenous dispersion of nanoparticles in the matrix. In this study, a series of agglomeration-free nano-WC-Co-reinforced 420 stainless steel matrix nanocomposite powders with high flowability were prepared by ball milling under the optimal parameters. The effect of ball milling time on the properties of the composite powders was investigated. Excellent powder properties ensure the DED processing performance. Furthermore, the corresponding composites were fabricated by DED, and the effects of nano-WC-Co content on the properties of the composites were comprehensively investigated. The contact angles between the single pass cladding layer and the substrate change with increasing nano-WC-Co content (decrease from 127.38° to 113.07°). The different contact angles will significantly influence the quality of the multi-pass cladding layer. Furthermore, the addition of nano-WC-Co leads not only to further grain refinement but also to more pronounced isotropy of the microstructure. With the increase in nano-WC-Co content, the corrosion

resistance is significantly improved (62.28% lower corrosion current for 420–15 wt% nano-WC-Co than for 420).

Keywords Steel matrix composites; Direct energy deposition (DED); Ball milling time; Contact angle; Microstructure; Mechanical property

1 Introduction

The 420 stainless steel is widely used in dies and molds because of its high Cr content and medium C content [1]. However, due to the interaction of the die with solids and liquids during repeated stamping, the surfaces of the die guide abrasives suffer from wear and erosion. These phenomena can lead to loss of function and failure of the die, thus reducing its service life. The addition of ceramic particles to metal matrix to form metal matrix composites (MMCs) has proven to be a viable and reliable method to enhance the wear and erosion resistance of materials [2–5]. Direct energy deposition (DED) is considered to be one of the most advantageous methods for preparing MMCs. Stainless steel nanoceramic composites are widely used in DED manufacturing due to their excellent performance and low cost [6–8]. However, compared to micron particles, the agglomeration tendency of nanoceramic particles is obvious due to van der Waals forces [9]. The agglomeration of ceramic particles will affect the continuity, uniformity and stability of composite powder during conveying, and thus affect the quality of formed parts. Therefore, the uniformity of nanoceramic particles in composite powder is the crucial factor to ensure the good performance of formed parts.

Ertugrul et al. [10] proposed the utility of high-energy ball milling (mechanical alloying) to solve the

Supplementary Information The online version contains supplementary material available at <https://doi.org/10.1007/s12598-023-02267-3>.

Z. Wang, S.-R. Xu, Q.-X. Sui, J. Wang, B. Liu, H. Wen, T.-Y. Xiao, Q. Yuan, F.-J. Zhao, J. Liu*
School of Materials Science and Engineering, Central South University, Changsha 410083, China
e-mail: liujun4982004@csu.edu.cn

J. Wang
Jinchuan Nickel Cobalt Research and Design Institute, Jinchuan Group Co., Ltd, Jinchang 737100, China



agglomeration problem of sub-micrometer or nano-sized ceramic particles in metal matrix composite powder. The milling process contributes to dispersing the nanoceramic particles and makes the nanoceramic powder attached onto metal powder. However, the ball milling process may adversely affect the shape and size of composite powder. The nanoceramic particles cannot be evenly attached to metal powder when the ball milling time is too short. Nevertheless, the shape and purity of composite powder may be changed when the ball milling time is too long. Wang et al. [11] pointed out that metal nanocomposite powder prepared under the optimum ball milling process also had the best performance of formed parts. This indicates that the ball milling process determines not only the properties of the composite powder but also the properties of the parts. Therefore, the selection of the ball milling process is crucial for the preparation of metal nanocomposite powder and subsequent formed parts. As far as the research on the preparation of DED metal matrix composites is concerned, most research has been carried out on surface strengthening [12–16]. The good compatibility of the coating with the substrate is the prerequisite for surface strengthening. The size of the contact angle reflects the compatibility between the coating and the substrate. However, the effect of content of ceramic particle on the contact angle between coating and matrix has not been reported.

Based on the above problems, 420 stainless steel nanocomposites with different mass fractions of nano-WC-Co particles for DED were prepared by ball milling method in this study. The effects of ball milling time and WC-Co content on the properties of composite powder were investigated. By studying morphology, chemical composition and properties of the composite powders, the optimum ball milling time of the composite powder with different contents of nano WC-Co was determined, respectively. The 420 stainless steel composite cladding layers containing 0 wt%, 5 wt%, 10 wt% and 15 wt% nano WC-Co particles were prepared by DED. The contact angle, phase composition and microstructure evolution of the composites with different nano-WC-Co contents were analyzed. The relationship between contact angle and cladding layer quality and the correlation between the content of WC-Co and mechanical properties were revealed.

2 Experimental

2.1 Powder preparation

The spherical 420 stainless steel powder with particle size in the range of 75–150 nm (Fig. 1a) was produced by gas

atomization method by Jiangsu Vilory Advanced Materials Technology Co., Ltd. Irregularly shaped nano-WC-Co particles with particle size in the range of 80–100 nm (Fig. 1b) were provided by HWNANO. The process of preparing 420-nano-WC-Co composite powder based on high-energy ball milling is shown in Fig. 1c. Three different 420-nano-WC-Co composite systems containing 5 wt%, 10 wt%, 15 wt% nano WC-Co particles (further named MMCs-1, MMCs-2, MMCs-3) were prepared. According to the previous study [17], the carbide balls with three different diameters were used as milling media. The diameters of the carbide balls were 3, 5 and 8 mm, respectively, and the mass ratio of the three kinds of cemented carbide balls was 2:3:5. The parameters of ball milling process are shown in Table 1 (where BPR is ball to powder ratio). In order to make nano-WC-Co particles evenly attached on the surface of 420 stainless steel, the ball milling process adopts the form of positive and reverse alternation, and stops for 10 min after 30 min positive rotation and then reverses for 30 min.

2.2 Direct energy deposition process

The 420-nano-WC-Co composite powders were deposited on the 316L stainless steel substrate by DED technology. The processing parameters of single pass cladding layer were selected as follows: single pass height of 3 mm, layer thickness of 0.2 mm, laser power of 900 W, scanning speed of $400 \text{ mm}\cdot\text{min}^{-1}$, powder feeding speed of $4.97 \text{ g}\cdot\text{min}^{-1}$ and argon flow rate of $5.0 \text{ L}\cdot\text{min}^{-1}$. The processing parameters of multi-pass cladding layer were the same as that of single pass cladding layer. The reciprocating scanning mode was adopted, and the cladding layer size was $30 \text{ mm} \times 20 \text{ mm} \times 10 \text{ mm}$ with a 50% lap ratio. The single pass cladding layers were mainly used for the analysis of contact angle, microstructure and hardness. Multi-pass cladding layers were mainly used for tensile, wear and corrosion resistance tests. Furthermore, 420 stainless steel cladding layers were prepared with the same parameters for reference.

2.3 Powder characterization

In order to determine the optimal ball milling time for preparing composite powder with different nano-WC-Co contents, the characteristics of composite powder were analyzed. The morphology of the composite powder was observed by scanning electron microscope (SEM, TESCAN MIRA3) equipped with energy-dispersive spectrum analyzer (EDS), and the adhesion of nano WC-Co particles on the surface of 420 stainless steel particles was analyzed. The shape of the composite powder was studied by a laser particle shape analyzer. The flow ability and density of

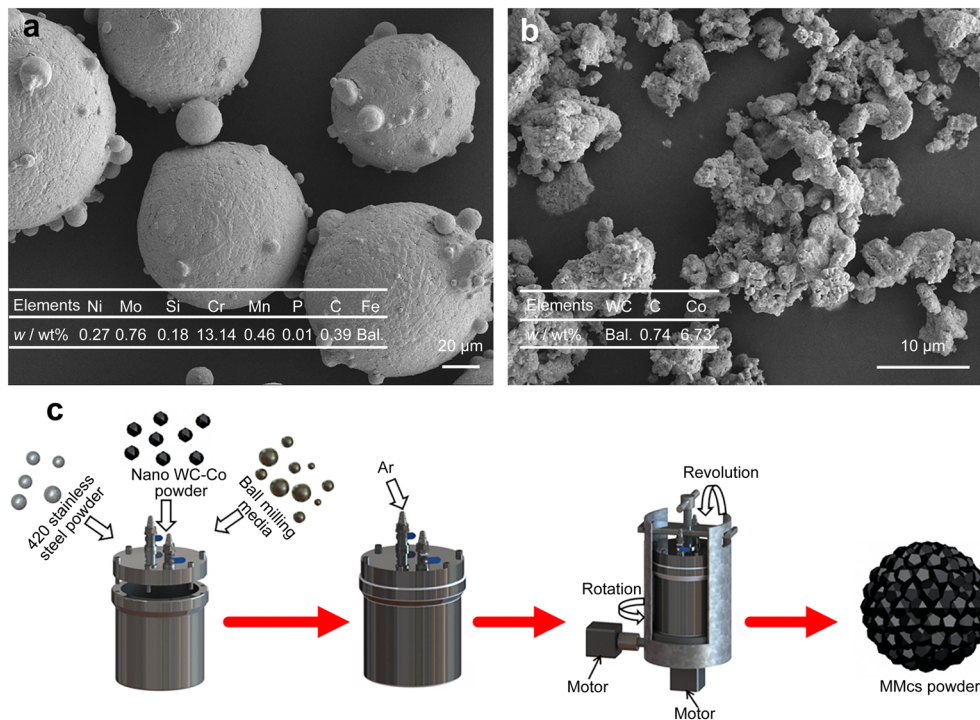


Fig. 1 **a** SEM image of 420 stainless steel powder; **b** SEM image of nano-WC-Co particles; **c** schematic diagram of preparation of 420-nano-WC-Co composite powder

Table 1 Parameters of processes with different ball milling time

Samples	BPR	Rotation speed / (r·min ⁻¹)	revolution speed / (r·min ⁻¹)	Milling time / h
MMCs-1	5:1	120	1	3
	5:1	120	1	6
	5:1	120	1	9
MMCs-2	5:1	120	1	9
	5:1	120	1	12
	5:1	120	1	15
MMCs-3	5:1	120	1	9
	5:1	120	1	12
	5:1	120	1	15

composite powder were measured with a Hall flowmeter and a tap density meter, respectively. The above analysis was used to determine the optimum ball milling time for the composite powders with different WC–Co contents. The composite powder after the optimum ball milling time was inlaid, and the inlaid samples were ground and polished to observe the cross-sectional morphology of the composite powders. The surface and cross section of the composite powder were observed by SEM equipped with an elemental mapping detector to verify the uniformity of the nano WC–Co particles attached to the surface of 420 stainless steel particles under the optimum ball milling time.

2.4 Cladding layer characterization

2.4.1 Morphology and microstructure

The single pass cladding layers were cut from the substrate by a wire cutting machine, and then, samples were cut along the deposition direction. The samples were ground and polished, and then used to analyze the effects of nano-WC–Co content on the morphology, microstructure and phase of the cladding layer. The overall morphology of the cross section of the single pass cladding layer was observed with an optical microscope (OM, SOPTOP CX40M), and the relevant characteristic values were measured to calculate the contact angle. The polished samples were etched using a solution consisting of HCl, anhydrous alcohol and CuCl₂ in order to observe the microstructure of the cladding layer along the deposition direction. The microstructure and element distribution of the cladding layer were further analyzed by SEM and EDS. X-ray diffraction (XRD, Rigaku SmartLab) and electron back scattered diffraction (EBSD) were used to analyze the phase composition and content of samples.

2.4.2 Characterization of properties

In this study, the hardness, tensile, wear and corrosion resistance of cladding layers with different WC–Co contents were mainly investigated. The Vickers hardness tester

was used to measure the hardness along the laser deposition direction with 0.2 mm as the measurement unit. During the hardness test, each sample was measured 10 times to obtain the average value, the load was 10 N and the loading time was 10 s. Tensile samples were sampled along the scanning direction of the multi-pass cladding layer. Tensile tests were carried out with displacement rate of 0.2 mm·min⁻¹ at room temperature using a universal testing machine. To ensure the reliability of the data, three tensile tests were performed for each group of tensile samples. The dry wear tests were performed at room temperature under a load of 5 N, using 6.35 mm diameter GCr15 balls as the wear medium. The wear time for each sample was 20 min while maintaining a frequency of 2 Hz and a sliding length of 10 mm. The corrosion experiment was carried out with a three-electrode system for electrochemical corrosion. The electrolyte was 3.5% NaCl solution.

3 Results and discussion

3.1 Composite powder characteristics

Figure 2 shows SEM images of MMCs-1, MMCs-2 and MMCs-3 under different ball milling time. It can be seen that ball milling time and nano-WC-Co content have an effect on the attachment of nano WC-Co particles in the composite powder. When the nano WC-Co content is 5 wt%, the nano WC-Co particles are all attached to 420 stainless steel particles after different ball milling time (Fig. 2a–c). However, as the content of nano-WC-Co particles increased, unattached nano WC-Co particles (marked with white circles) in the form of agglomerates appeared in both MMCs-2 and MMCs-3 after 9 and 12 h of ball milling (Fig. 2d, e, g, h). Shi and Wang [6] pointed out that the uniformity of nanoceramic particles coated on the surface of metallic spherical powder was an important indicator for the preparation of metallic nanocomposite powder. In order to verify whether nano-WC-Co particles are evenly attached to 420 stainless steel particles, EDS-point analysis of MMCs-1, MMCs-2 and MMCs-3 under different ball milling time was carried out. Figure 2 also shows the diffraction intensity of W, C and Co elements on the surface of each composite powder after different ball milling time. Although nano-WC-Co particles in MMCs-1 are all attached to the surface of 420 stainless steel particles after different ball milling time, the distribution of nano-WC-Co particles is very different. Among them, the elements distribution difference of nano-WC-Co particles in MMCs-1 after 3-h ball milling is the largest, and that after 6-h ball milling are the smallest. Owing to the presence of unattached WC-Co nanoparticles in MMCs-2 and MMCs-

3 after 9- and 12-h ball milling, there are differences in the diffraction intensity of the EDS elements at different positions in the composite powder. In contrast, after 15 h of ball milling, all the nano-WC-Co particles are attached to the surface of 420 powder in MMCs-2 and MMCs-3, and there is no significant difference in their EDS elemental diffraction intensity. It means that nano-WC-Co particles are evenly attached to the surface of 420 particles in MMCs-2 and MMCs-3 after ball milling of 15 h. Results of SEM images and EDS-points illustrate that elemental distribution of nano-WC-Co particles in MMCs-1, MMCs-2 and MMCs-3 is the most uniform after 6, 15 and 15 h of ball milling, respectively.

For metal nanocomposite powder, in addition to a uniform distribution of nano particles on the surface of the metal particles, the composite powder is required to have a good shape, flowability and high tap density. Figs. S1–S3 respectively plot the particle shape distribution curves of MMCs-1, MMCs-2 and MMCs-3 under different ball milling time. Table 2 lists the circularity, Hall flow rate and tap density of the composite powder with different ball milling time and different nano-WC-Co contents, respectively. It can be observed that the MMCs-1, MMCs-2 and MMCs-3 after 6, 15 and 15 h ball milling, respectively, present the best powder performance. This indicates that the coating uniformity of nanoceramic particles on the metal surface determines the properties of metal nanocomposite powder.

It can be concluded from the above study that after 6-, 15- and 15-h ball milling, respectively, the nano-WC-Co particles of MMCs-1, MMCs-2 and MMCs-3 not only attached to the 420 surface uniformly, but the composite powder presented the best morphology and properties. To further illustrate the attachment effect of nano-WC-Co in each composite powder at the optimum ball milling time, elemental mapping of the surface and cross section of each composite powder were carried out. In the mapping of elements on the surface of each composite powder, the W, C and Co are uniformly distributed on the surface of the 420 stainless steel spherical powder (Fig. 3). The same phenomenon can be seen in the elemental mapping of the cross section of each composite powder. As shown in the elemental mapping of the cross section of each composite powder (Fig. 3), the composite powder forms a core-shell structure and the thickness of the shell increases with the increase in nano-WC-Co content. In summary, after 6, 15 and 15 h of ball milling, respectively, MMCs-1, MMCs-2 and MMCs-3 all exhibited good performance.

It is clear that the composite powder prepared with the optimal ball milling time has the best properties. And the morphology of the powder was improved to some extent during the ball milling process compared to the initial powder morphology (Fig. 1a). Based on previous studies

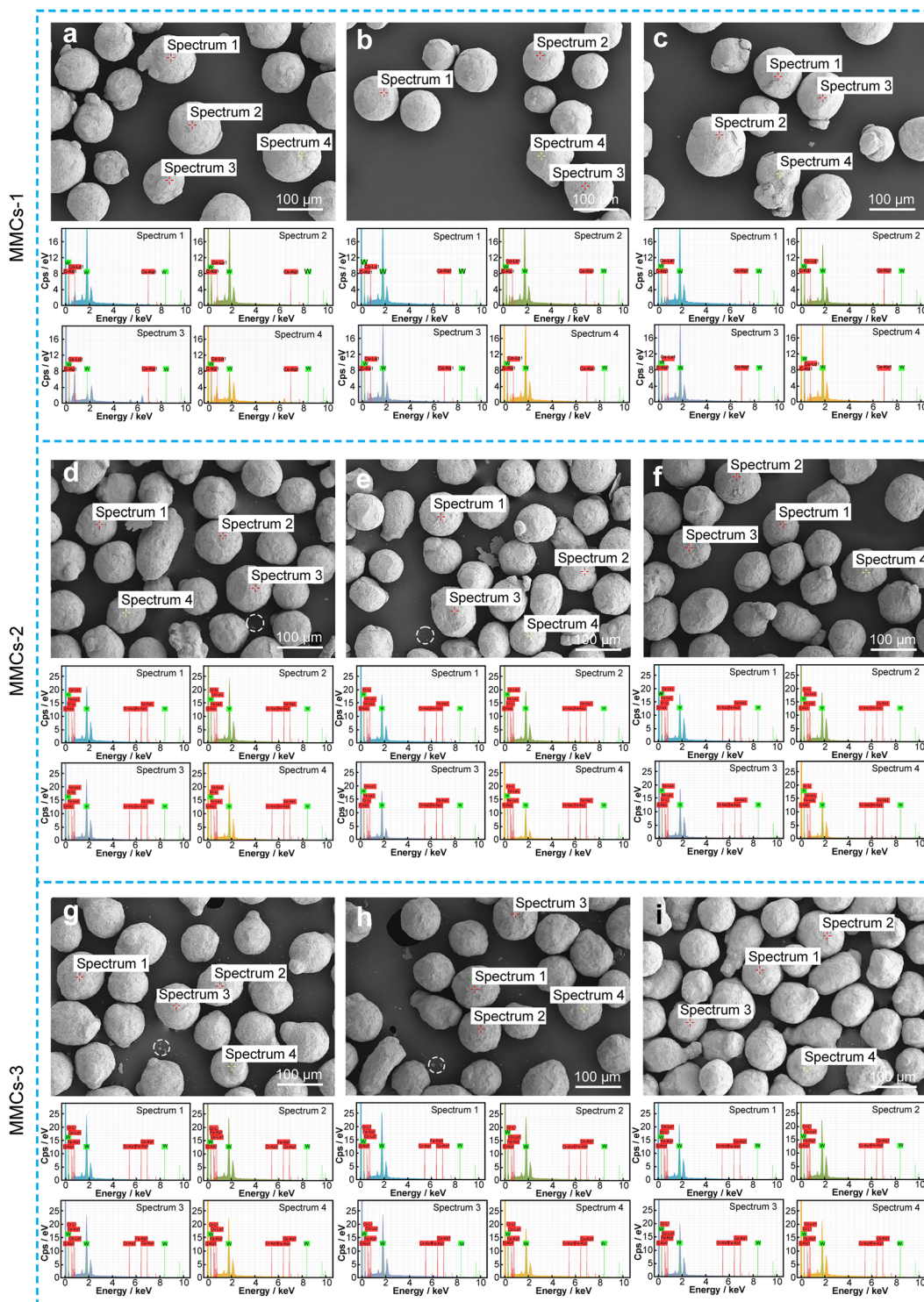


Fig. 2 SEM images and EDS point analysis of ball milled samples: MMCs-1 for **a** 3 h, **b** 6 h and **c** 9 h; MMCs-2 for **d** 9 h, **e** 12 h and **f** 15 h; MMCs-3 for **g** 9 h, **h** 12 h and **i** 15 h

about the effect of ball milling parameters on the quality of powder and formed part, the uniformity of ceramic particles in composite and optimal powder properties are the prerequisite to ensure the performance of samples in

additive manufacturing (AM) process [8, 11, 18]. Therefore, the composite powder prepared under optimal ball milling parameters possesses the best powder performance and performance of the formed part simultaneously. In the



Table 2 Powder characteristics of MMCs-1 after different ball milling time

Samples	Ball milling time / h	Circularity	Hall flow rate / (50 g·s ⁻¹)	Tap density / (g·cm ⁻³)
MMCs-1	3	0.9010	18.70	4.76
	6	0.9100	16.46	5.06
	9	0.9007	18.82	4.88
MMCs-2	9	0.8764	17.98	4.57
	12	0.8990	17.45	4.76
	15	0.9012	17.35	4.78
MMCs-3	9	0.8811	20.12	4.76
	12	0.8977	19.67	4.82
	15	0.8982	18.58	4.88

following section, the performance of the parts by DED utilizing composite powder prepared under the optimal ball milling parameters will be investigated.

3.2 Morphological features and microstructure of cladding layers

The contact angle is a pivotal parameter reflecting the compatibility between matrix and cladding material. The contact angle can be calculated using the following equation [19]:

$$\theta = 2\arctan(2H/W) \quad (1)$$

where θ is the contact angle; H is the height of single-pass cladding; W is the width of single-pass cladding.

Figure 4a schematically shows the geometric characteristics of a single pass cladding along the deposition direction. Figure 4b–d shows the morphology of single pass cladding layers along the deposition direction of MMCs-1, MMCs-2 and MMCs-3, respectively. It can be seen from the morphology of each single pass that WC–Co is extremely sensitive to the contact angle. When the content of nano-WC–Co particles increases from 5 wt% to 10 wt%, the contact angle changes significantly, and the contact angle decreases from 127.38° to 114.02°. When the content of nano-WC–Co particles increases to 15 wt%, the contact angle changes moderately, and the contact angle decreases from 114.02° to 113.07°. Owing to the high laser absorption rate of WC and uniform coating of nano-WC–Co particles on the surface of 420 stainless steel particles, the addition of nano WC–Co particles will increase the temperature of the molten pool. The increase in molten pool temperature will reduce the surface tension of molten metal, which results in the reduction in the contact angle between matrix and cladding layer. Oliveira et al. [20] pointed out that a small contact angle could ensure a good metallurgical bond, but a small contact angle might cause gaps between passes in the multi-pass cladding process, which would form holes and cracks in the final cladding layer. Those holes and cracks

deteriorate the quality of DED formed parts. Therefore, contact angle larger than 100° benefits better performance of formed parts. Although the contact angle between the single pass cladding layers and the matrix is greater than 100°, the decrease in the contact angle still has a certain effect on the multi-pass cladding layer. As shown in Fig. 4e–h, with the addition of nano-WC–Co particles, the defects in the multi-pass cladding layer become more obvious. When the content of nano WC–Co particles is 5 wt% whose contact angle is 127.38°, there are tiny holes with average hole size of 25.92 μm (Fig. 4f) in the multi-pass cladding layer. When the content of nano-WC–Co particles increases to 10 wt%, the contact angle is 114.02°, the holes in multi-pass cladding layer become larger and cracks appear (Fig. 4g). The average hole size in MMCs-2 multi-pass cladding layer is 84.70 μm , in comparison that in the MMCs-3 multi-pass cladding layer is 42.12 μm (Fig. 4h). Although the contact angle of MMCs-3 is smaller than that of MMCs-2, the average size of holes in multi-pass cladding layer of MMCs-3 is smaller. This can be ascribed to the higher tap density of MMCs-3 than that of MMCs-2, and the tap density is the key factor to ensure the density of DED formed parts. Wang et al. [21] investigated the performance of formed parts of the same powder prepared for DED in different ways separately, and the results showed that the higher the tap density of the powder is, the higher the density of formed parts is. Therefore, the higher tap density of MMCs-3 powder endues the formed part with a higher density than that of MMCs-2.

The micromorphology of the single pass composite cladding layers along the deposition direction was observed by SEM with back scattered electron detector. The addition of nano-WC–Co particles leads to precipitation of phases concentrated at grain boundaries, which are used to prevent grain growth in the composite cladding layer (Fig. 5). The more the nano-WC–Co particles, the more obvious the precipitated phase and the smaller grain size of the cladding layer is. Therefore, the introduction of nano WC–Co induces the obvious grain refinement effect

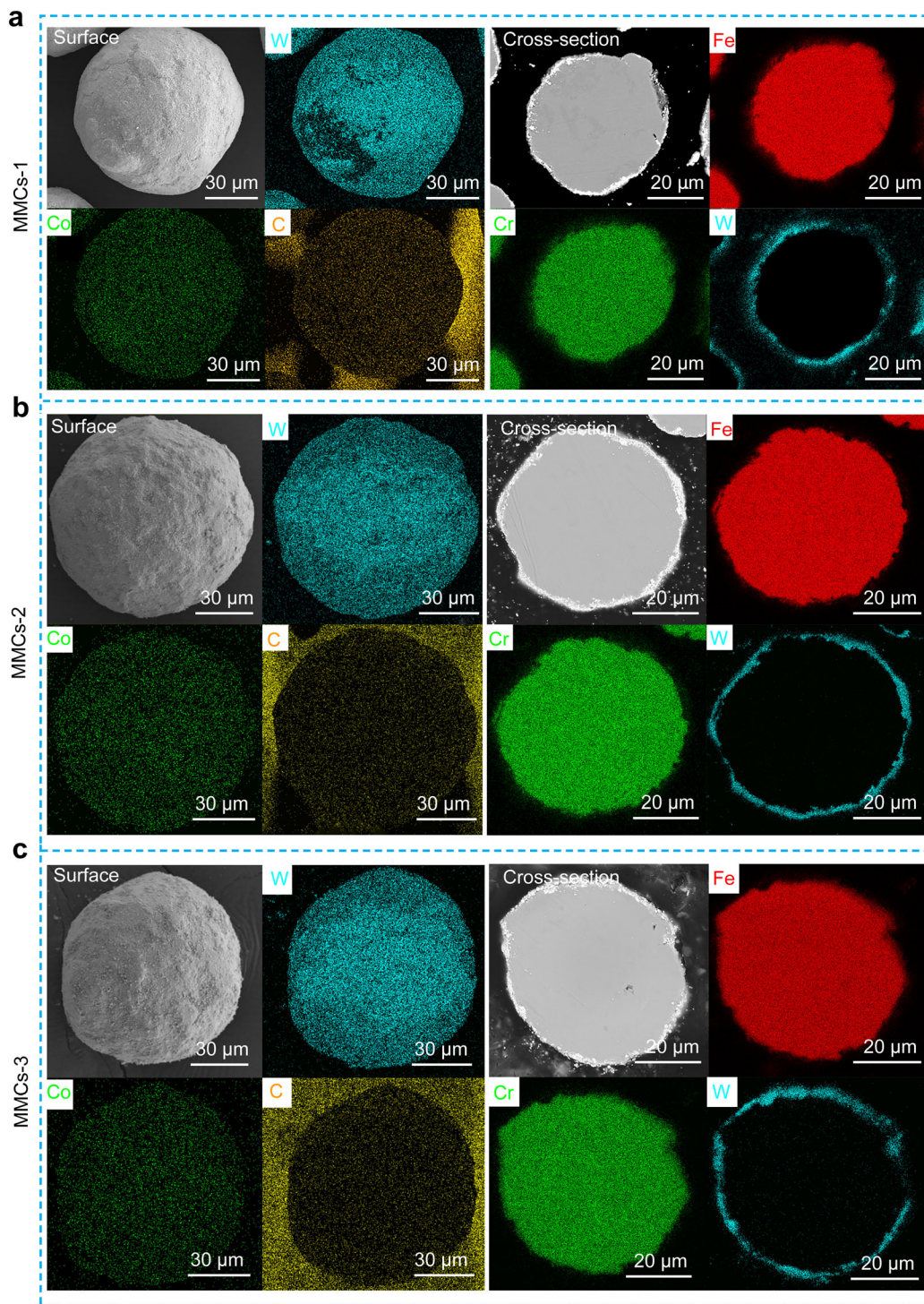


Fig. 3 Element mapping of surfaces and cross sections of **a** MMCs-1, **b** MMCs-2 and **c** MMCs-3 after 6, 15 and 15 h of ball milling, respectively

of Fe-based materials. Chen et al. [7] found that in the process of powder bed fusion (PBF), a large amount of C in WC diffused into the iron base matrix, and a large amount of diffused C dissolved in the iron base matrix in the form of interstitial atoms. These diffused C atoms form (Fe,

W)_xC type carbide with Fe and W elements. Figure 5 shows the elements mapping in each cladding layer. The C atom of WC diffuses in the cladding layer, so it can be inferred that the precipitates at grain boundaries are (Fe, W)_xC carbides. Figure 5 also shows EDS spectrum

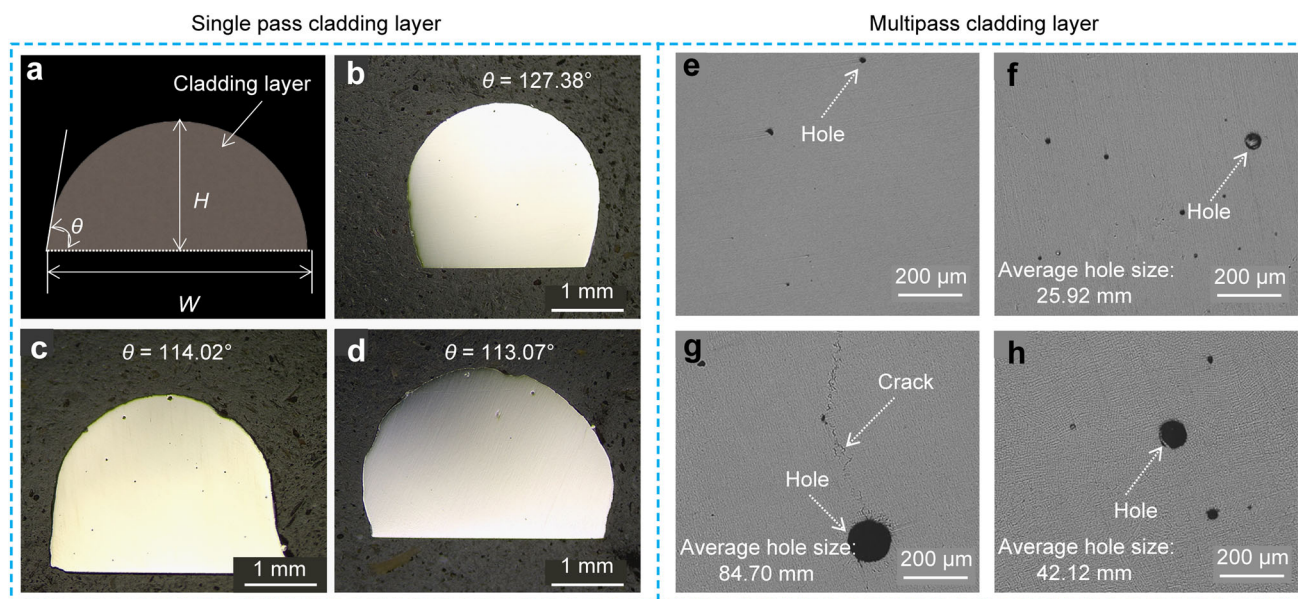


Fig. 4 Cross-sectional morphology of single pass cladding layer: **a** geometric characteristics of single pass, **b** MMCs-1, **c** MMCs-2 and **d** MMCs-3; cross-sectional morphology of multi-pass cladding layers: **e** 420 stainless steel, **f** MMCs-1, **g** MMCs-2 and **h** MMCs-3

corresponding to positions marked with red cross in each cladding layer. The EDS spectra demonstrate that with the increase in nano-WC-Co content, the W content in the precipitated phase increases, while the content of Fe element decreases. Therefore, the atomic ratio of Fe and W in the precipitated phase varies is related to the mass fractions of nano-WC-Co.

XRD patterns of the powder and cladding layers are given in Fig. 6. Compared with powder (Fig. 6a), the phase of cladding layers has changed significantly. Figure 6b shows XRD patterns of the cladding layers of 420, MMCs-1, MMCs-2 and MMCs-3. α -Fe is the dominant phase within the microstructure of 420 cladding layer since 420 stainless steel is martensite steel. However, the addition of nano-WC-Co will produce γ -Fe phase in the cladding layer. The strong diffraction corresponding to α -Fe and weak diffraction corresponding to γ -Fe in MMCs-1 cladding layer are detected. As the content of nano-WC-Co is increased to 10 wt%, the strong diffraction corresponding to γ -Fe and weak diffraction corresponding to α -Fe in MMCs-2 cladding layer are detected. With the further increase in nano-WC-Co content, the diffraction intensity corresponding to α -Fe becomes weaker and diffraction peaks of $\text{Fe}_3\text{W}_3\text{C}$ and $\text{Fe}_2\text{W}_2\text{C}$ carbides in the MMCs-3 cladding layer are detected. The increase in nano-WC-Co particles changed the microstructure of 420 stainless steel matrix from martensite to austenite. The diffraction corresponding to WC cannot be detected in the XRD patterns of MMCs-1, MMCs-2 and MMCs-3, indicating that the nano-WC-Co particles have undergone a complete dissolution within the 420 stainless steel matrix during the DED.

The complete dissolution of nano-WC-Co will increase the content of carbon in the molten pool, thus reducing the initial temperature of martensite transition and hindering the martensite transition. Through element mapping (Fig. 5), it can be seen that C atoms are dispersed in the cladding layer, and the diffused carbon atoms are dissolved in the matrix in the form of interstice atoms, thus affecting the phase transformation of 420 matrix between austenite and martensite. In addition, DED process is a non-equilibrium process under rapid cooling, in which the 420 stainless steel matrix is in a supersaturated state and can no longer directly dissolve more W and C atoms into the matrix. Therefore, excess W and C precipitate as additional carbide phases. The carbide precipitated phase in the composite cladding layer is $\text{Fe}_3\text{W}_3\text{C}$ and $\text{Fe}_2\text{W}_2\text{C}$ carbides. These carbides in MMCs-1 and MMCs-2 cladding layer cannot be identified by XRD due to their low volume fraction.

To further illustrate the phase distribution and microstructure of formed part, EBSD analysis was carried out along the deposition direction of the samples. The corresponding phase maps, orientation maps and pole figure (PF) maps are shown in Fig. 7. The austenite content in composites increases significantly with the increase in nano-WC-Co particle content as shown in phase maps. The austenite distribution in MMCs-1 is uniform, and the volume fraction is 41.8%. When the content of nano-WC-Co is 10 wt%, the austenite content increases significantly, and the volume fraction increases to 74.9%. While the content of nano-WC-Co further increases to 15 wt%, the cladding layer is almost austenite and the volume fraction of

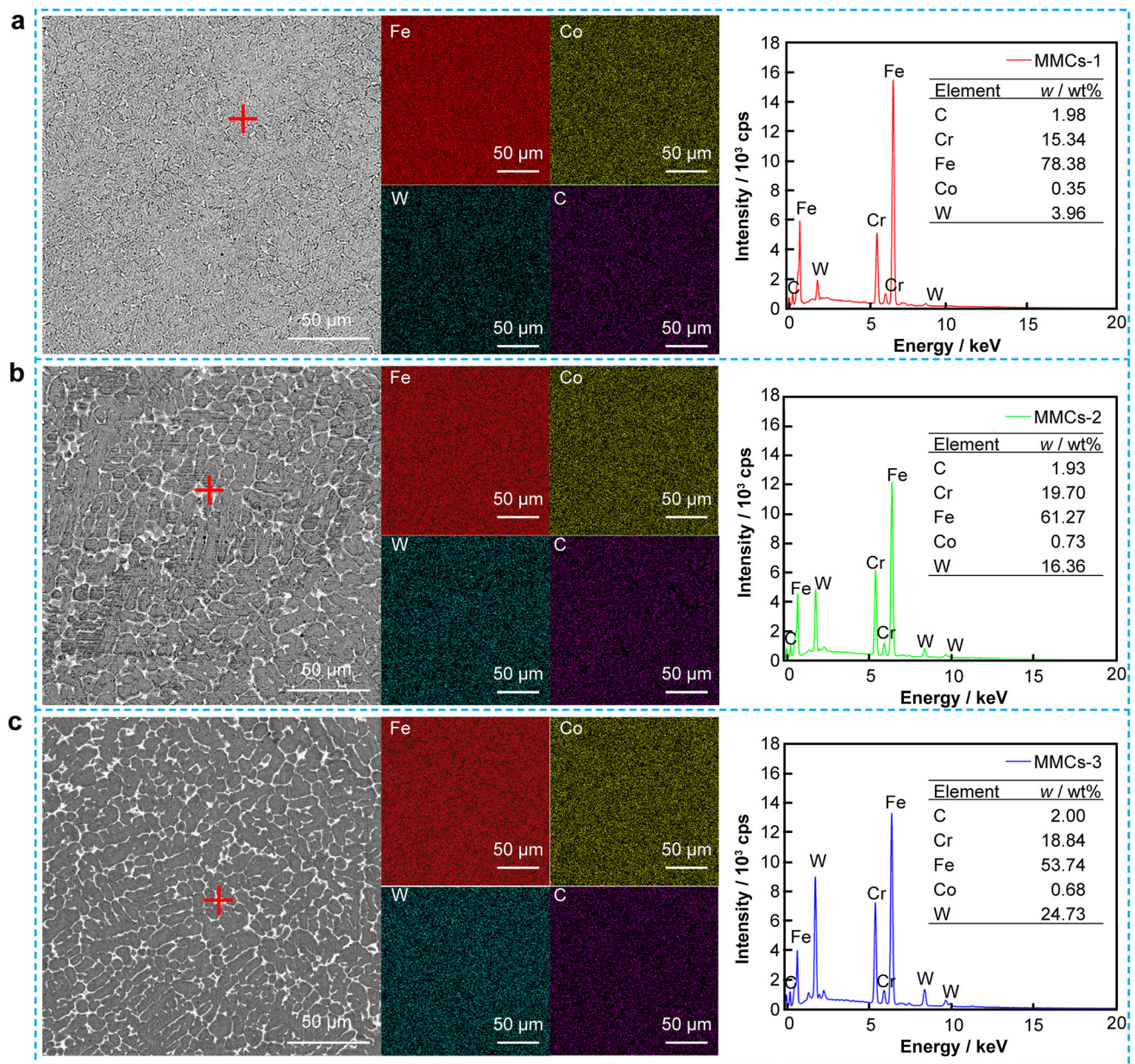


Fig. 5 SEM images, mapping and EDS analysis results of composite cladding layer: **a** MMCs-1; **b** MMCs-2; **c** MMCs-3

austenite in MMCs-3 is 99.3%. The observation is consistent with XRD analysis of the cladding layers (Fig. 6b). According to EBSD orientation maps of nano-WC-Co particles with different additive amounts, it can be found that the introduction of nano-WC-Co particles has a significant effect on grain refinement of 420 stainless steel matrix. This finding is consistent with the microstructure of the cladding layer (Fig. 5). Zhai et al. [22] confirmed that the addition of ceramic particles would change the microstructure of iron matrix and serve as heterogeneous nucleation sites during solidification, leading to grain refinement. The lath martensite structure can be clearly observed in the microstructure of the composites with 5 wt%

nano-WC-Co, and the lath martensite becomes shorter and narrower with the increase in nano-WC-Co mass fraction. After the addition of 15 wt% nano-WC-Co particles, the grain morphology of MMCs-3 exhibits significant difference from that of MMCs-1 and MMCs-2. The martensite lath in the MMCs-3 almost disappeared, and a higher isotropic feature of the iron matrix was obtained, as indicated by the continuous color change in the orientation diagram. The PF maps quantify the texture strength of the austenite phase along $\langle 100 \rangle$, $\langle 110 \rangle$ and $\langle 111 \rangle$ crystal orientations relative to the upper surface of the prepared each sample. From the phase maps that austenite is the main phase of the composite structure, only the PF maps of austenite are

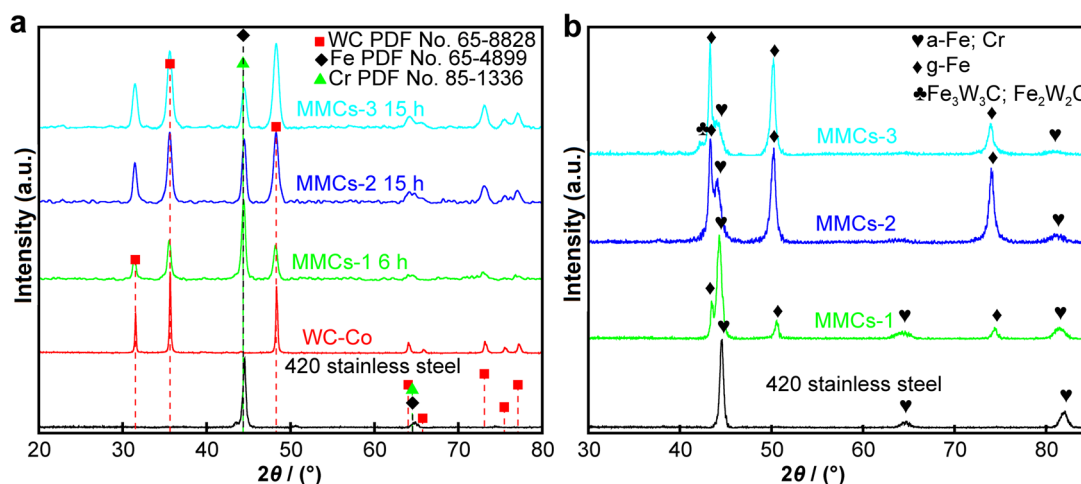


Fig. 6 XRD patterns of **a** composite powder and **b** cladding layer

given. In MMCs-1, the austenite microtexture is low, and only the $\langle 100 \rangle$ and $\langle 111 \rangle$ textures are detected (Exp. density_{max} = 6.76). When the content of nano-WC-Co particles increases to 10 wt%, the intensity of texture of $\langle 100 \rangle$ and $\langle 111 \rangle$ increases (Exp. density_{max} = 10.15). However, MMCs-3 has more uniform grain direction distribution and lower convergence (Exp. density_{max} = 4.81) than MMCs-1 and MMCs-2, which confirms that austenite grains have high isotropy characteristics. Chen et al. [7] showed that the higher the WC content was, the more obvious the isotropic structure of composites was. However, compared with PBF technology, the microstructure of ceramic particles steel matrix composites prepared by DED exhibits obvious isotropy. As studied by Zhai et al. [22], ceramic particles act as nucleating agents during solidification. From the point of view of thermodynamics, a slower cooling rate can increase nucleation rate [23]. However, in PBF and DED, the cooling rate is too large, leading to the opposite relationship between the degree of undercooling and the nucleation rate. The nucleation rate decreases with the increase in cooling rate. Compared with PBF, the cooling rate of DED is relatively slow, so more nuclei form in the composite material, which ultimately leads to more obvious isotropy of the material.

3.3 Properties of cladding layers

The average hardness of the single pass cladding layer of 420 stainless steel, MMCs-1, MMCs-2 and MMCs-3 is shown in Fig. 8a. The addition of WC particles has been found in numerous studies to be effective in increasing the microhardness of the clad layer. Surprisingly, the addition of WC/WC-Co particles will reduce the average hardness of the cladding layer in this study [24–27]. Mola et al. [28]

found that the volume fraction of martensite in the mixture of martensite and austenite determined its hardness. From the phase maps of EBSD analysis (Fig. 7), the volume fraction of austenite in the cladding layer increases with the increase in the content of nano-WC-Co particles. Therefore, the decrease in martensite content in cladding layer leads to the decrease in hardness of cladding layers. When the content of nano-WC-Co particles increases to 15 wt%, the volume fraction of martensite in the cladding is the lowest (Fig. 7c), but the diffraction peaks of carbides appear in the MMCs-3 cladding layer (Fig. 6b), and the precipitation of carbides would increase the hardness of the cladding layer. Therefore, the hardness of MMCs-3 cladding layer is improved.

Figure 8b shows the tensile yield strength of all tensile samples at room temperature. Compared with the tensile properties of the samples without nano-WC-Co particles, the tensile properties of the samples with nano-WC-Co particles are greatly reduced. The significant reduction in tensile yield strength indicates that the incorporation of WC-Co nanoparticles transforms the material from a ductile to a brittle material. The tensile fracture mechanism is shown in Fig. S4. According to the literature, the strength and ductility of metal matrix composites can be improved simultaneously by (i) grain refinement [29], (ii) non-equilibrium grain boundaries [30] and (iii) precipitation of nanoscale particles [31]. However, this is not applicable to the composite prepared in this study. This illustrates that the strength and ductility of stainless steel nanocomposites may depend mainly on the combined effect of the types of the stainless steel and ceramic particles.

In Fig. 8c, the results of wear tests at room temperature are presented. According to the modified empirical equation [32]:

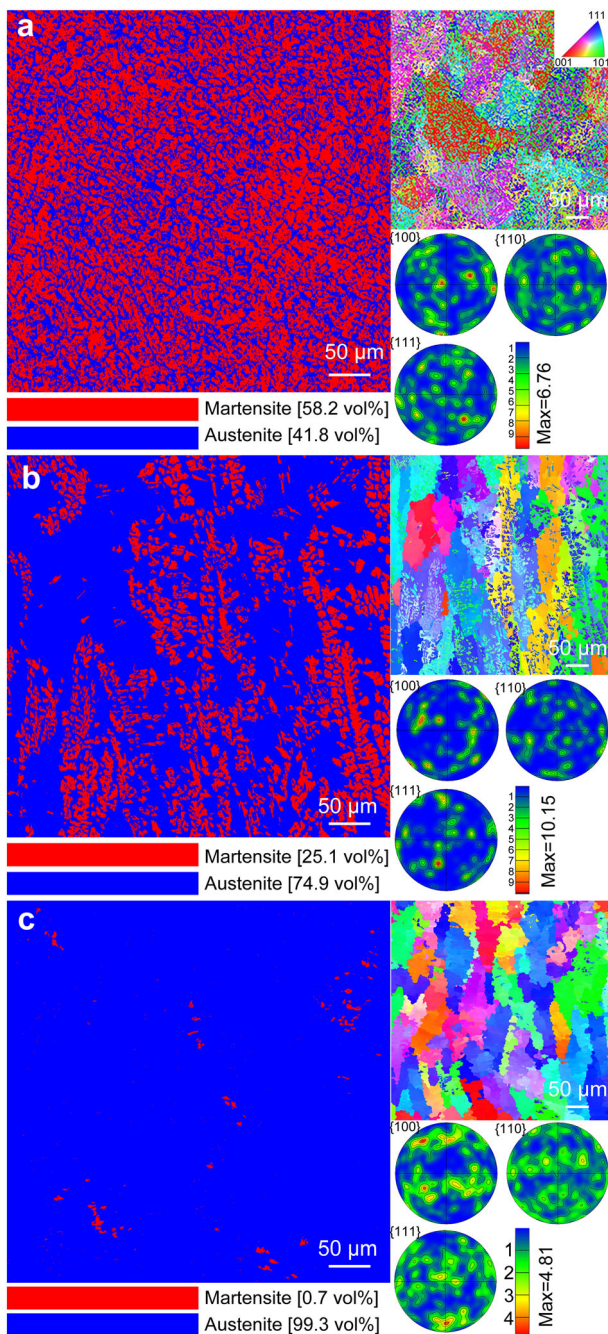


Fig. 7 Phase map of EBSD analysis of **a** MMCs-1, **b** MMCs-2 and **c** MMCs-3

$$W = k \left(\frac{P}{H} \right) \quad (2)$$

where W is the wear rate, P is the applied load, H is the material hardness, k is the pre-factor related to the material ductility. When k and P are constants, increasing microhardness can improve wear performance.

As shown in Fig. 8a, 420 stainless steel has the highest hardness, but its wear performance is not the best. When the content of nano-WC-Co particles is 15 wt%, the friction coefficient is the lowest, indicating that the wear performance is the best. It has been pointed out that the precipitation of carbide [33], the refinement of microstructure [34] and the improvement of microhardness [35] jointly improve wear performance. As shown in Fig. 5, with the increase in nano-WC-Co particles content, the amount of precipitated carbides at grain boundary increases and the grain of cladding layer is further refined. Through this study, it can be seen that grain refinement and carbide precipitation are more effective in improving the wear resistance of composites than increasing hardness. However, MMCs-2 exhibits worse wear properties than the 420 stainless steel matrix. According to the literature [36–38], the degree of densification has a certain influence on the wear properties of composites. The densification degree of MMCs-2 is the lowest due to the large pores and cracks in MMCs-2 (Fig. 4g). Therefore, MMCs-2 has the worst wear performance. The wear mechanism is illustrated in Fig. S5.

The corrosion current can be used to evaluate the corrosion resistance of the alloys. Figure 8d shows the corrosion current of the cladding layer with different mass fractions of nano-WC-Co in the potential range from -1.6 to 0.4 V. The 420 stainless steel cladding layer has a larger corrosion current, while the composite cladding layers with different mass fractions nano-WC-Co particles have a smaller corrosion current. The decrease in corrosion current means the improvement of corrosion resistance. This indicates that the addition of nano-WC-Co particles improves the corrosion resistance of the cladding layer. The corrosion current of MMCs-2 increases due to more defects in the cladding layer. Although the corrosion current of MMCs-2 increases, the corrosion current of MMCs-2 is less than that of 420 stainless steel cladding layer. When the nano-WC-Co particles content is 15 wt%, the corrosion current is the smallest, meaning the best corrosion resistance of the cladding layer. According to the study of Zhang and Kovacevic [14], the addition of WC will harm the corrosion resistance of 420 stainless steel. This is contrary to the results obtained in this study. Owing to the high density of WC particles, micron WC particles mostly deposited in the bottom of the coating layer, which reduce corrosion resistance. In this study, nano-WC-Co particles are evenly distributed in the cladding layer (Fig. 5), thus playing a protective role on 420 stainless steel matrix. Therefore, the uniform distribution of nanoceramic particles can effectively improve the corrosion resistance of composites.

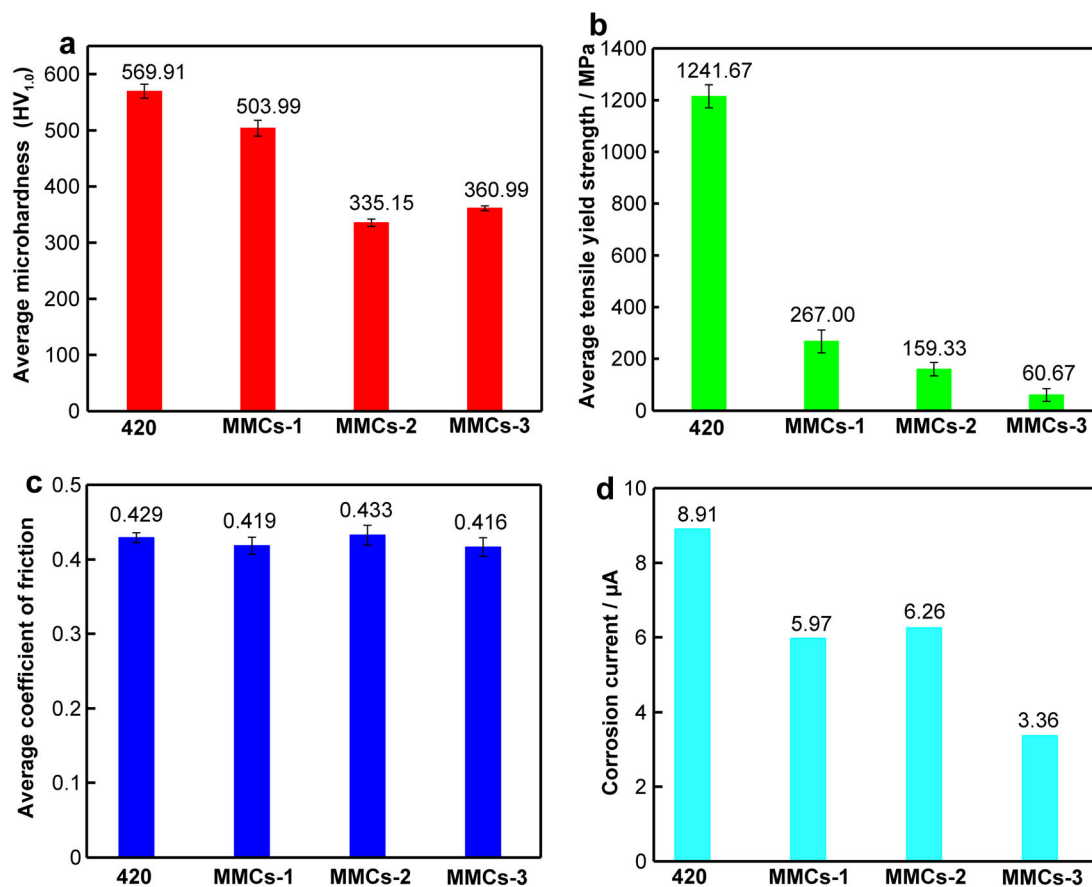


Fig. 8 a Average hardness, b average tensile yield strength, c average coefficient of friction and d corrosion current of 420 stainless steel and composite cladding layers

4 Conclusion

MMCs-1, MMCs-2 and MMCs-3 composite powder with good powder properties were prepared by ball milling process under the optimum ball milling time, respectively. Then, the single-pass and multi-pass cladding layers were prepared by DED technology. The composite powder has optimal powder properties when the nano-WC-Co particles are uniformly adhered to the spherical surface of 420 stainless steel. The addition of nano-WC-Co particles results in a significant change of the contact angle between the composite cladding layer and the matrix. The decrease in contact angle increases the possibility of defects in the multi-pass composite cladding layer. The incorporation of nano-WC-Co particles not only has a vital grain refinement effect in the microstructure of the composite cladding layer, but also has a significant effect on the isotropy of the composite cladding layer. The addition of nano-WC-Co particles greatly influences the mechanical properties of cladding layers. Compared with those of 420 stainless steel cladding layer, the hardness and tensile yield strength of composite cladding layers are decreased. The fracture of cladding layer changes from ductile fracture to brittle

fracture. However, the addition of nano-WC-Co can effectively improve the wear and corrosion resistance of cladding layer.

Acknowledgements This study was financially supported by Gansu Science and Technology Department (No. 21ZD3GC001).

Declarations

Conflict of interests The authors declare that they have no conflict of interest.

References

- [1] Nath SD, Clinning E, Gupta G, Poirier VW, Espérance G, Gulsoy O, Kearns M. Effects of Nb and Mo on the microstructure and properties of 420 stainless steel processed by laser-powder bed fusion. *Addit Manuf.* 2019;28:682. <https://doi.org/10.1016/j.addma.2019.06.016>.
- [2] Sadoun AM, Najjar IR, Alsorjji GS, Abd-Elwahed MS, Elaziz MA, Fathy A. Utilization of improved machine learning method based on artificial hummingbird algorithm to predict the tribological behavior of Cu-Al₂O₃ nanocomposites synthesized by in situ method. *Mathematics.* 2022;10(8):1266. <https://doi.org/10.3390/math10081266>.

- [3] Zhang RY, Li JX, Yang S, Yan H, Liu H, Zhao G. Microstructure and corrosion resistance of TiB₂(p)/ZL205 composites with different TiB₂ conten. *Chin J Rare Met.* 2021; 45(2):194. <https://doi.org/10.13373/j.cnki.cjrm.xy19060027>.
- [4] Wang T, Liu XY, Chen SY, Lei JB, Song XL. Study on microstructure and tribological properties of nano/micron TiC/TC4 composites fabricated by laser melting deposition. *J Manuf Process.* 2022;82:296. <https://doi.org/10.1016/j.jmapro.2022.07.068>.
- [5] Sadoun AM, Najjar IMR, Abd-Elwahed MS, Meselhy A. Experimental study on properties of Al-Al₂O₃ nanocomposite hybridized by graphene nanosheets. *J Mater Res Technol.* 2020; 9(6):14708. <https://doi.org/10.1016/j.jmrt.2020.10.011>.
- [6] Shi J, Wang Y. Development of metal matrix composites by laser-assisted additive manufacturing technologies: a review. *J Mater Sci.* 2020;55:9883. <https://doi.org/10.1007/s10853-020-04730-3>.
- [7] Chen HY, Gu DD, Zhang HM. Novel WC-reinforced iron-based composites with excellent mechanical properties synthesized by laser additive manufacturing: underlying role of reinforcement weight fraction. *J Mater Process Tech.* 2021;289:116959. <https://doi.org/10.1016/j.jmatprotec.2020.116959>.
- [8] Wang X, Zhang ZH, Men YZ, Li XJ, Liang YH, Ren LQ. Fabrication of nano-TiC functional gradient wear-resistant composite coating on 40Cr gear steel using laser cladding under starved lubrication conditions. *Opt Laser Technol.* 2020;126:106136. <https://doi.org/10.1016/j.optlastec.2020.106136>.
- [9] Hao XN, Liu X. Molecular dynamics study on microscale residual stress of graphene/aluminum nanocomposites by selective laser sintering. *Rare Met.* 2022;41(11):3677. <https://doi.org/10.1007/s12598-022-02079-x>.
- [10] Ertugrul O, Enrici TM, Paydas H. Laser cladding of TiC reinforced 316L stainless steel composites: feedstock powder preparation and microstructural evaluation. *Powder Technol.* 2020;375:384. <https://doi.org/10.1016/j.powtec.2020.07.100>.
- [11] Wang RQ, Xi LX, Gökce B, Barcikowski S, Gu DD. Powder preparation during ball milling and laser additive manufacturing of aluminum matrix nanocomposites: powder properties, processability and mechanical property. *Adv Powder Technol.* 2022;8(33):103687. <https://doi.org/10.1016/j.apt.2022.103687>.
- [12] Bartkowski D, Bartkowska A, Jurči P. Laser cladding process of Fe/WC metal matrix composite coatings on low carbon steel using Yb: YAG disk laser. *Opt Laser Technol.* 2021;136:106784. <https://doi.org/10.1016/j.optlastec.2020.106784>.
- [13] Chen H, Lu YY, Sun YS. Coarse TiC particles reinforced H13 steel matrix composites produced by laser cladding. *Surf Coat Tech.* 2020;395:125867. <https://doi.org/10.1016/j.surfcoat.2020.125867>.
- [14] Zhang Z, Kovacevic R. Laser cladding of iron-based erosion resistant metal matrix composites. *J Manuf Process.* 2019;38:63. <https://doi.org/10.1016/j.jmapro.2019.01.001>.
- [15] Tian ZH, Zhao YT, Jiang YJ, Ren HP. Microstructure and properties of Inconel 625 + WC composite coatings prepared by laser cladding. *Rare Met.* 2021;40(8):2281. <https://doi.org/10.1007/s12598-020-01507-0>.
- [16] Chen LY, Zhao Y, Meng FW, Yu TB, Ma ZL, Qu S, Sun ZY. Effect of TiC content on the microstructure and wear performance of in situ synthesized Ni-based composite coatings by laser direct energy deposition. *Surf Coat Technol.* 2022;444:128678. <https://doi.org/10.1016/j.surfcoat.2022.128678>.
- [17] Wang Z, Tan MX, Wang J, Zeng J, Zhao FJ, Xiao XY, Xu SR, Liu B, Gong L, Sui QX, Zhang RZ, Han B, Liu J. Core-shell structural iron based metal matrix composite powder for laser cladding. *J Alloys Compd.* 2021;878:160127. <https://doi.org/10.1016/j.jallcom.2021.160127>.
- [18] Zhu HM, Ouyang MN, Hu JP. Design and development of TiC-reinforced 410 martensitic stainless steel coatings fabricated by laser cladding. *Ceram Int.* 2021;9(47):12505. <https://doi.org/10.1016/j.ceramint.2021.01.108>.
- [19] Zhou SW, Xu TY, Hu C. Utilizing carbon nanotubes in ceramic particle reinforced MMC coatings deposited by laser cladding with Inconel 625 wire. *J Mater Res Technol.* 2021;13:2026. <https://doi.org/10.1016/j.jmrt.2021.06.028>.
- [20] Oliveira U, Ocelík V, De Hosson JThM. Analysis of coaxial laser cladding processing conditions. *Surf Coat Tech.* 2005; 197(2–3):127. <https://doi.org/10.1016/j.surfcoat.2004.06.029>.
- [21] Wang Z, Wang J, Xu SR, Liu B, Sui QX, Zhao FJ, Gong L, Liu J. Influence of powder characteristics on microstructure and mechanical properties of Inconel 718 superalloy manufactured by direct energy deposition. *Appl Surf Sci.* 2022;583:152545. <https://doi.org/10.1016/j.apsusc.2022.152545>.
- [22] Zhai WG, Zhu ZG, Zhou W, Nai SML, Wei J. Selective laser melting of dispersed TiC particles strengthened 316L stainless steel. *Compos Part B Eng.* 2020;199:108291. <https://doi.org/10.1016/j.compositesb.2020.108291>.
- [23] Chen HY, Gu DD, Kosiba K, Lu TW, Deng L, Xi LX, Kühn U. Achieving high strength and high ductility in WC-reinforced iron-based composites by laser additive manufacturing. *Addit Manuf.* 2020;35:101195. <https://doi.org/10.1016/j.addma.2020.101195>.
- [24] Benarji K, Ravikumar Y, Jinoop AN, Paul CP, Bindra KS. Effect of WC composition on the microstructure and surface properties of laser directed energy deposited SS 316-WC composites. *J Mater Eng Perform.* 2021;30:6732. <https://doi.org/10.1007/s11665-021-05971-2>.
- [25] Hosseini-Tayeb H, Rafiaei SM. Enhanced microstructural and mechanical properties of stellite/wc nanocomposite on Inconel 718 deposited through vibration-assisted laser cladding. *Int J Miner Metall Mater.* 2022;29:327. <https://doi.org/10.1007/s12613-020-2211-0>.
- [26] Wang T, Zhu L, Song HY, Wang H. Effect of WC-17Co content on microstructure and properties of IN718 composites prepared by laser cladding. *Opt Laser Technol.* 2022;148:107780. <https://doi.org/10.1016/j.optlastec.2021.107780>.
- [27] Liu SF, Li YZ, Wang Y, Yk W, Zhang LL, Wang JY, Yang X. Selective laser melting of WC-Co reinforced AISI 1045 steel composites: microstructure characterization and mechanical properties. *J Mater Res Technol.* 2022;19:1821. <https://doi.org/10.1016/j.jmrt.2022.05.158>.
- [28] Mola J, Seo EJ, Cho L. Correlation between mechanical stability and hardness of austenite in martensite/austenite mixtures. *Mater Sci Eng A.* 2021;822:141687. <https://doi.org/10.1016/j.msea.2021.141687>.
- [29] Xu SP, Shi CS, Zhao NQ, He CN. Microstructure and tensile properties of A356 alloy with different Sc/Zr additions. *Rare Met.* 2021;40(9):2514. <https://doi.org/10.1007/s12598-020-01529-8>.
- [30] Chen W, Xu LY, Hao KD, Han YD, Zhao L, Jing HY. Additive manufacturing of 15–5PH/WC composites with the synergistic enhancement of strength and ductility. *Mater Sci Eng A.* 2022; 840:142926. <https://doi.org/10.1016/j.msea.2022.142926>.
- [31] Chen HY, Lu TW, Wang YG, Liu Y, Shi TY, Prashanth KG, Kosiba K. Laser additive manufacturing of nano-TiC particles reinforced CoCrFeMnNi high-entropy alloy matrix composites with high strength and ductility. *Mater Sci Eng A.* 2022;833:142512. <https://doi.org/10.1016/j.msea.2021.142512>.
- [32] Gu DD, Ma J, Chen HY, Lin KJ, Xi LX. Laser additive manufactured WC reinforced Fe-based composites with gradient reinforcement/matrix interface and enhanced performance. *Compos Struct.* 2018;192:387. <https://doi.org/10.1016/j.compstruct.2018.03.008>.



- [33] Zhu CB, Fordyce L, Sun SD, Annasamy M, Fabijanic D, Short K, Paradowska A, Leary M, Brandt M, Easton M. Effect of Ti and TiC additions on the microstructure and wear resistance of high chromium white irons produced by laser directed energy deposition. *Wear*. 2022;510–511:204519. <https://doi.org/10.1016/j.wear.2022.204519>.
- [34] Yi JL, Niu B, Pan LL, Zou XD, Cao Y, Wang X, Luo JW, Hu YJ. Influence of WC grain size on the microstructure and wear property enhancement of 18Ni300 coatings. *Surf Coat Technol*. 2022;447:128823. <https://doi.org/10.1016/j.surfcoat.2022.128823>.
- [35] Zhou L, Zhang JW, Li SQ, Tian Y, Wang JP, Huang MY, Yuan Q, Li X, Kou ZL, Zhan GD, He DW. Effects of hardness and grain size on wear resistance of polycrystalline cubic boron nitride. *Int J Refract Hard Mater*. 2022;836:142574. <https://doi.org/10.1016/j.msea.2021.142574>.
- [36] Xie HB, Zhang JL, Li FL, Yuan GQ, Zhu Q, Jia QL, Zhang HJ, Zhang SW. Selective laser melting of SiCp/Al composites: densification, microstructure, and mechanical and tribological properties. *Ceram Int*. 2021;21(47):30826. <https://doi.org/10.1016/j.ceramint.2021.07.263>.
- [37] Chen L, Sun YZ, Li L, Ren YP, Ren XD. In situ TiC/Inconel 625 nanocomposites fabricated by selective laser melting: densification behavior, microstructure evolution, and wear properties. *Appl Surf Sci*. 2020;518:145981. <https://doi.org/10.1016/j.apsusc.2020.145981>.
- [38] Xie HB, Zhang JL, Li FL, Yuan GQ, Zhu Q, Jia QL, Zhang HJ, Zhang SW. Selective laser melting of SiCp/Al composites: densification, microstructure, and mechanical and tribological properties. *Ceram Int*. 2021;47(21):30826. <https://doi.org/10.1016/j.ceramint.2021.07.263>.

Springer Nature or its licensor (e.g. a society or other partner) holds exclusive rights to this article under a publishing agreement with the author(s) or other rightsholder(s); author self-archiving of the accepted manuscript version of this article is solely governed by the terms of such publishing agreement and applicable law.